

Journal Pre-proofs

On bio-MOF materials doped with phosphorescent iridium complexes for molecular oxygen determination: synthesis, characterization and performance

Jiali Xie, Xiang Chen, Huanrong Li, Zhenbo Chen

PII: S1386-1425(21)00618-1
DOI: <https://doi.org/10.1016/j.saa.2021.120041>
Reference: SAA 120041

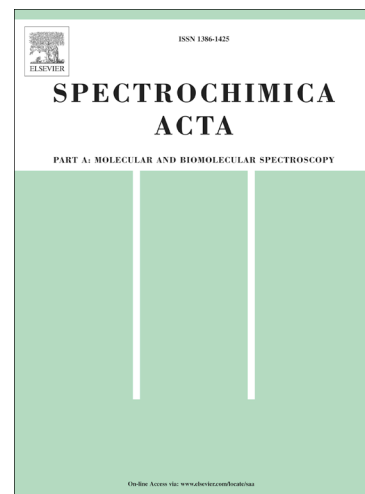
To appear in: *Spectrochimica Acta Part A: Molecular and Biomolecular Spectroscopy*

Received Date: 12 March 2021
Revised Date: 24 May 2021
Accepted Date: 30 May 2021

Please cite this article as: J. Xie, X. Chen, H. Li, Z. Chen, On bio-MOF materials doped with phosphorescent iridium complexes for molecular oxygen determination: synthesis, characterization and performance, *Spectrochimica Acta Part A: Molecular and Biomolecular Spectroscopy* (2021), doi: <https://doi.org/10.1016/j.saa.2021.120041>

This is a PDF file of an article that has undergone enhancements after acceptance, such as the addition of a cover page and metadata, and formatting for readability, but it is not yet the definitive version of record. This version will undergo additional copyediting, typesetting and review before it is published in its final form, but we are providing this version to give early visibility of the article. Please note that, during the production process, errors may be discovered which could affect the content, and all legal disclaimers that apply to the journal pertain.

© 2021 Published by Elsevier B.V.



On bio-MOF materials doped with phosphorescent iridium complexes for molecular oxygen determination: synthesis, characterization and performance

Jiali Xie Data curation Writing - review & editing^a, Xiang Chen Data curation formal analysis^b, Huanrong Li Investigation Supervision^{a,*}, Zhenbo Chen Investigation Supervision^{b,*}, chenzb981@163.com

^aDepartment of Chemistry, Renmin University of China, Beijing, 100872, P. R. China

^bDepartment of Chemistry, Capital Normal University, Beijing 100048, P. R. China

*Corresponding author.

Graphical abstract

Highlight

Two phosphorescent Ir(III) complexes were synthesized and doped into a supporting matrix of bio-MOF-1 via cationic exchange.

Their phosphorescent emission was confirmed by density functional theory and emission lifetime, making them applicable for oxygen sensing.

Linear working curves were observed for both composite samples, showing sensitivity as high as 23.65 with response/recovery time of 9/22 seconds.

Humidity effect on sensing performance was limited.

Abstract

In this paper, two phosphorescent Ir(III) complexes, Ir(ppy)₂(Ln), were synthesized using 2-phenyl pyridine (ppy) as the first (major) ligand and two phosphorous compounds (L1 and L2) as the auxiliary ligand. Their single crystal structure and electronic structure were discussed. Ir(ppy)₂(Ln) complexes were doped into a

supporting matrix of bio-MOF-1 via cationic exchange to ensure their uniform distribution. Their successful doping was confirmed by SEM, fluorescence microscopy image, XRD, N₂ adsorption/desorption and ICP measurement. Their photophysical parameters, including absorption spectra, excitation spectra, emission spectra, emission lifetime and quantum yield, were discussed in detail. Their phosphorescent emission was confirmed by density functional theory and emission lifetime, making them applicable for oxygen sensing. Linear working curves were observed for both composite samples, showing sensitivity as high as 23.65 with response/recovery time of 9/22 seconds. Humidity effect on sensing performance was limited. These parameters were found superior to literature ones based on phosphorescent Cu(I), RE(III), Ru(II) and Re(I) complexes. The sensing mechanism was revealed as a dynamic collision between Ir(ppy)₂(Ln) and O₂ molecules. The novelty of this work was the combination of phosphorescent Ir(III) complexes with porous bio-MOF-1, resulting in greatly improved sensitivity and linear sensing with short response time.

Keywords:

O₂ sensing, phosphorescent Ir(III), bio-MOF-1, emission quenching

1. Introduction

There are multiple physiological, biological and pathological activities that need molecular oxygen (O_2), which consequently makes O_2 an important analytical target. O_2 concentration determination and identification are considered important in various fields, such as analytical diagnostics, food industry, medical analysis, industrial packaging, electronics industry, automotive industry and environmental protection [1,2]. The accurate O_2 determination can be finished via modern analytical methods, such as electrochemical method, chemical titration and optoelectronic detection [3]. Among these proposed detection methods for O_2 determination, optical sensing has attracted much research interest, owing to its virtues of fast response, low consumption, economic cost and simple operation [4]. For most luminescence-based O_2 sensing approaches, there are two major structural/functional components, which are sensing probe and its supporting host, respectively. Both components have to comply with some criteria to ensure desired sensing performance.

As for an oxygen sensing probe, its oxygen quenching behavior affects sensing performance the most. Many sensing probes have been reported for oxygen sensing, such as organic dyes, metallic porphyrins (Pt), Ru(II) complexes and Ir(III) complexes [5-8]. Particularly, Ir(III) complexes have shown promising performance owing to their virtues of highly phosphorescent structure at room temperature, long excited state lifetime and broad distribution of excited electrons, which endows them with desired features for oxygen sensing [8]. For example, Liu and coworkers have reported bis-cyclometalated diphenylamino-based Ir(III) complexes with sensing sensitivity (I_0/I_{100})

of ~ 16 , using ethyl cellulose film as supporting host [9]. Xing and coworkers have reported Ir(III) complexes with carbazole-derived ligands, showing a highest I_0/I_{100} value of ~ 168.6 [10]. By combining two emission bands from a coumarin dye and a red-emitting Ir(III) complex, ratiometric oxygen sensing has been reported by Yoshihara and coworkers [11].

The supporting host serves as a gas-penetrable matrix to allow the collision between O_2 molecules and sensing probe. As a consequence, its microenvironment plays an important role in controlling response/recovery behavior and even the linearity of working curve [12]. Generally, good gas diffusion rate and linear working curve depend on rigid micropores with uniform distribution and size homogeneity. As a consequence, further research effort has been focused on the exploration of excellent supporting host. For example, polymers, such as polystyrene, poly(cyclohexene carbonate) and poly(dimethylsiloxane), have been tried as the supporting host owing to their good compatibility with Ir complexes [13-15]. Silica-based supporting matrix, such as MCM-41 and SBA-15, have been widely studied owing to their stable microstructure [16,17]. Never the less, these candidate hosts generally won't satisfy both rigid uniform microstructure and high gas diffusion rate, compromising sensing sensitivity and the linearity of working curve.

The development of metal-organic framework (MOF) materials has offered a new choice for supporting platform [18,19]. They are usually nanocrystal structures with variable building components, resulting in rigid and controllable micropores for sensing application. A representative example, bio-MOF-1, is reported by Rosi and coworkers

with molecular composition of $\text{Zn}_8(\text{ad})_4(\text{BPDC})_6\text{O} \cdot 2\text{Me}_2\text{NH}_2$ [20]. Except for its rigid and uniform micropores, bio-MOF-1 has an additional advantage as follows. There is a counterion $(\text{Me}_2\text{NH}_2)^+$ in bio-MOF-1, which makes its modification/doping easy to be done via a simple ionic exchange procedure.

In this work, we intend to construct an oxygen sensing system by combining phosphorescent Ir(III) complex (sensing probe) with bio-MOF-1 (supporting platform). We decide to use 2-phenyl pyridine (ppy) as the first ligand and two phosphorous ligands (L1 and L2) as the auxiliary ligand to form Ir(III) dopant of $\text{Ir}(\text{ppy})_2(\text{Ln})$, as shown in Scheme 1. To ensure the uniform distribution of Ir(III) dopant in bio-MOF-1 matrix, we used solution-soaking method, hoping to construct a promising oxygen sensing platform with high sensitivity, fast response/recovery response and linear working curve.

2. Experimental section

2.1 Reagents

The synthetic method for Ir(III) dopant (denoted as $\text{Ir}(\text{ppy})_2(\text{Ln})$, $n=1,2$) and the construction route for Ir(III)-doped bio-MOF-1 (denoted as $\text{Ir}(\text{ppy})_2(\text{Ln})@$ bio-MOF, $n=1,2$) are shown in Scheme 1. All chemical reagents used in Scheme 1 were bought from Tianjin Chemical Cooperation and used as received, including bis(2-(diphenylphosphanyl)phenyl) ether (L1), triphenylphosphane (L2), 2-phenyl pyridine (ppy), KPF_6 , $\text{IrCl}_3 \cdot 3\text{H}_2\text{O}$, zinc acetate dihydrate, adenine and 1,4-benzenedicarboxylic acid.

2.2 Characterization methods

MS, ICP and NMR data were collected on a Bruker Avance 500 spectrometer, a Hitachi P-4010 spectrometer and an Agilent 1100 MS spectrometer, respectively. A Bruker SMART APEX II X-ray single crystal diffractometer was applied to collect single crystal diffraction data of Ir(III) complexes, using graphite-monochromated Mo K α radiation at 293 K. All hydrogen atoms were calculated. For ORTEP plotting, *telp* was set as 30. SEM and fluorescence microscopy images were taken from a S4800 microscope and a Hitachi fluorescence microscope, respectively. ICP data were provided by a Hitachi P-4010 spectrometer. A Shimadzu UV-3101PC spectrophotometer and a Hitachi F-7000 fluorescence spectrophotometer were applied to determine absorption spectra and emission spectra, along with emission lifetime and quantum yield. A CHI660C electrochemical workstation was selected to evaluate sample electrochemical data, using a working electrode of Pt plate, a counter electrode of Pt mesh and a reference electrode of saturated calomel electrode (SCE). Redistilled CH₃CN was used as solution with sample concentration of 1 mM and supporting electrode of tetrabutylammonium hexafluorophosphate (0.1 M). Every solution was bubbled with pure N₂ stream for 10 minutes to remove dissolved O₂.

Density functional theory (DFT) calculation was carried out on Ir(III) single crystals at RB3LYP/LANL2DZ level with GAMESS, using their single crystal structures as initial geometry. The graphical presentation for frontier molecular orbitals (FMOs) was finished by wxMacMolPlt with contour value of 0.03. For oxygen sensing performance discussion, pure N₂ and pure O₂ streams were controlled with gas flow meters and mixed together in a gas chamber which was finally connected to a quartz chamber to

record emission spectra. As for humidity experiment, hot water steam from a steam generator was mixed with atmosphere-controlling gas and then guided into a condenser pipe (20°C) to generate water-saturated gas (relative humidity=100%). All measurements were carried out in the air at room temperature (293 K) without being specified.

2.3 Synthesis of Ir(ppy)₂(L1) and Ir(ppy)₂(L2)

Ir(III) dimer was synthesized prior to use following below method. A mixture of IrCl₃·3H₂O (1.5 mmol), ppy (3.0 mmol), 2-ethoxyethanol (30 mL) and pure water (10 mL) was stirred and then heated to reflux under N₂ atmosphere. After being heated for 24 hours, this solution was cooled to room temperature and mixed with 20 mL of pure water. Solid product was obtained as Ir(III) dimer. This Ir(III) dimer was mixed with L1 ligand (3.0 mmol), MeOH (10 mL) and CH₂Cl₂ (20 mL). After being heated at 90°C for 24 hours, this solution was cooled to room temperature and mixed with KPF₆ (15 mmol). Solid product was obtained after being stirred for 3 hours. This crude product was purified by recrystallization in MeOH. Ir(ppy)₂(L1) was finally obtained as a white solid. Yield (50%). ¹H NMR (DMSO-d₆) δ 8.84-8.81 (m, 2H), 8.41-8.38 (m, 2H), 8.25-8.22 (m, 2H), 7.80-7.76 (m, 4H), 7.39-7.36 (m, 30H), 7.13-7.10 (m, 4H). ¹³C NMR (DMSO-d₆) δ 164.12, 160.50, 152.86, 152.13, 144.37, 142.44, 139.03, 138.56, 138.19, 133.34, 132.85, 129.34, 128.73, 125.46, 124.62, 123.65, 120.13, 116.49. ³¹P NMR (DMSO-d₆) δ -146.75, 39.24. ESI-MS: *m/z* = 1039.2. Ir(ppy)₂(L1) single crystal was obtained by vapor evaporation method.

Ir(ppy)₂(L2) was obtained using a similar method, but L2 ligand was used in this run.

$\text{Ir(ppy)}_2(\text{L2})$ was obtained as a white solid. Yield (49%). $^1\text{H NMR}$ (DMSO-d_6) δ : 8.82-8.79 (m, 2H), 8.43-8.41 (m, 2H), 8.26-8.22 (m, 2H), 7.80-7.78 (m, 4H), 7.48-7.46 (m, 21H). $^{13}\text{C NMR}$ (DMSO-d_6) δ : 161.60, 148.80, 142.68, 142.30, 139.29, 136.48, 134.32, 132.88, 129.88, 129.30, 126.23, 125.52, 120.57. $^{31}\text{P NMR}$ (DMSO-d_6) δ : 39.02. ESI-MS: $m/z = 798.3$. $\text{Ir(ppy)}_2(\text{L2})$ single crystal was obtained by vapor evaporation method.

2.4 Synthesis of $\text{Ir(ppy)}_2(\text{Ln})@$ bio-MOF

Prior to the loading procedure, supporting matrix bio-MOF-1 was synthesized following a literature procedure, with starting reagents of zinc acetate dihydrate, adenine and 1,4-benzenedicarboxylic acid [19]. After being washed by DMF, white needle crystals were obtained as bio-MOF-1 and dried in vacuum for 30 hours. Then $\text{Ir(ppy)}_2(\text{L1})$ and $\text{Ir(ppy)}_2(\text{L2})$ were doped into bio-MOF-1 via ionic exchange. A typical run was described as follows. The as-synthesized bio-MOF-1 (0.1 g) was mixed with DMF (15 mL) and 0.05 mmol of Ir(III) complex. After being stirred at room temperature for 2 days (300 rpm), solid sample was collected and washed with DMF and MeOH. Such ionic exchange reaction was performed 3 times under the same condition. White powder was finally obtained, denoted as $\text{Ir(ppy)}_2(\text{L1})@$ bio-MOF and $\text{Ir(ppy)}_2(\text{L2})@$ bio-MOF.

3. Results and discussion

3.1 Characterization on dopant Ir(III) complexes

3.1.1 Single crystal structure

As mentioned in the Experimental section, $\text{Ir(ppy)}_2(\text{L1})$ and $\text{Ir(ppy)}_2(\text{L2})$ were doped into bio-MOF-1 via ionic exchange procedure. To ensure the successful ionic exchange

reaction, there are counterions in these two Ir(III) complexes, PF_6^- and Cl^- . $\text{Ir}(\text{ppy})_2(\text{L1})$ and $\text{Ir}(\text{ppy})_2(\text{L2})$ single crystals were obtained (see Table S1, Supporting Information for detailed crystal information). Their ORTEP plotting is shown in Figure 1. The key crystal cell parameters listed in Table 1 suggest a monoclinic system with only one molecule in each cell unit. The cell length parameters listed in Table 1 suggest that both $\text{Ir}(\text{ppy})_2(\text{Ln})$ molecules are small enough to be doped into the micropores of bio-MOF-1 (~2 nm). Owing to the coordination affinity difference between C atom (from ppy), N atom (from ppy) and P atom (from L1/L2), a distorted coordination geometry is formed around Ir(III) center. In $\text{Ir}(\text{ppy})_2(\text{L1})$, there are two ppy ligands and one L1 ligand, which are all bidentate ligands, forming an octahedral field. Clearly, PF_6^- is not involved in the coordination geometry, merely serving as a counterion. On the other hand, in $\text{Ir}(\text{ppy})_2(\text{L2})$, except for two ppy ligands and one L2 ligand, there is still one Cl atom to form its octahedral field. Here the Cl atom coordinates with Ir(III) center, serving as both a counterion and a ligand. This Cl atom is not replaced by a L2 ligand due to the crowded environment around Ir(III) center. All Ir-C/Ir-N bond length values of $\text{Ir}(\text{ppy})_2(\text{L1})$ are found larger than those of $\text{Ir}(\text{ppy})_2(\text{L2})$. Additionally, these bond length values in Table 1 are larger than literature values of similar $\text{Ir}(\text{ppy})_2(\text{Ligand})$ complexes (<2.0 Å) [21,22]. Similar case is observed for Ir-Cl and Ir-P bonds. The Ir-Cl and Ir-P bonds in $\text{Ir}(\text{ppy})_2(\text{Ln})$ complexes (2.5 Å) are obviously longer than literature values of metal complexes with less crowded coordination environment (2.3 Å) [21,22]. It appears that L1 and L2 ligands bring a lot steric hindrance around Ir(III) center, which leads to a crowded coordination environment in $\text{Ir}(\text{ppy})_2(\text{L1})$ and $\text{Ir}(\text{ppy})_2(\text{L2})$ and

consequently weakened coordination bonds between Ir(III) center and ligands.

Except for its effect on bond length, the stretching and rotation movement of phenyl rings in L1 and L2 ligands prohibits Ir(ppy)₂(Ln) molecules from approaching to each other. In this case, there is no intermolecular π - π interaction in Ir(ppy)₂(L1) and Ir(ppy)₂(L2) crystals, as depicted by Figure 1. Even in packing mode, the shortest distance between every two Ir(ppy)₂(Ln) molecules is longer than 9.7 Å, as a consequence, the interaction between excited Ir(ppy)₂(Ln) molecules can be avoided, so that the aggregation-caused quenching effect shall be decreased, which is widely reported in Ir(III)-based emitters.

On the other hand, no obvious effect from the steric hindrance of Ln ligands on coordination bite angle of Ir(ppy)₂(Ln) is observed. It is observed from Table 1 that the coordination bite angle of ppy ligand (N-Ir-C angle) in Ir(ppy)₂(Ln) (~80 °) is similar to literature values of Ir(III) complexes with less crowded coordination environment (~79 °) [21,22]. Similarly, the coordination bite angle of L1 ligand in Ir(ppy)₂(L1) (~100 °) is similar to the natural distortion angle of free L1 ligand (~122 °). This result reveals that all ligands are trying to minimize the steric hindrance around coordination center by distorting their structures and moving far away from the Ir(III) center. This statement can be confirmed when comparing the increased Ir...O distance in Ir(ppy)₂(L1) (3.5 Å) with literature values (<3 Å).

3.1.2 DFT calculation

Generally, metal-to-ligand-charge-transfer (MLCT) transition has been confirmed oxygen-sensitive since the excited electrons are localized on π^* orbitals of ligands,

which makes them vulnerable to energy acceptors and thus can be efficiently quenched by O₂ molecules via a dynamic energy transfer mechanism [15-17]. To confirm the MLCT charge transfer in complexes, DFT calculation is applied to reveal the electronic transition between their frontier molecular orbitals (FMOs). The percentage composition of these FMOs is listed in Table 2 and Table 3. A graphic presentation for transition-involved FMOs, LUMO+1, LUMO, HOMO, HOMO-1, HOMO-2 and HOMO-3, is shown as Figure 2. As for the unoccupied FMOs of Ir(ppy)₂(Ln), dominant contribution from ppy ligand is observed. Considering the slim contribution from other structural components, these unoccupied FMOs are assigned as π* of ppy ligand. As for the occupied FMOs of Ir(ppy)₂(Ln), ppy contribution is greatly decreased, with Ir contribution increased obviously. The contribution from Ln ligand and Cl atom is generally lower than 20%. In this case, the onset electronic transitions between these FMOs shall be assigned with a MLCT character, which is consistent with literature reports [20,21]. As shown in Figure 2, the electrons of excited MLCT state are localized on the conjugation plane of ppy ligand. Upon an efficient collision with a proper energy acceptor, such as ³O₂, these excited electrons may lose their energy via a non-radiative path, leading to emission absence. This MLCT transition nature endows Ir(ppy)₂(Ln) with a possibility of being an oxygen sensing probe.

3.1.3 Electrochemistry property

Aiming at a better understanding on the structure-property relationship in Ir(ppy)₂(Ln), cyclic voltammetry (CV) is performed on Ir(ppy)₂(L1) and Ir(ppy)₂(L2), as shown in Figure S3 (Supporting Information). It is observed that Ir(ppy)₂(L1) shows

two weak peaks at 0.91 V and 1.26 V, which are attributed to the oxidation of Ir-C(ppy) and Ir-P(L1) groups. There is a strong peak at -1.12 V, which shall be attributed to the reduction of ppy ring. Similar three peaks are observed for Ir(ppy)₂(L2) as well. In addition, there is a strong peak at 1.64 V which shall be attributed to the oxidation of Cl⁻ ligand. The reduction current values of ppy ring in Ir(ppy)₂(L1) and Ir(ppy)₂(L2) are similar to each other, but the oxidation current of Ir-P(L1) group in Ir(ppy)₂(L1) is much weaker than that of Ir-P(L2) group in Ir(ppy)₂(L2). This is because Ir(ppy)₂(L1) is a cation and not easy to be oxidized, while Ir(ppy)₂(L2) is a neutral complex which is more easily to be oxidized.

3.2 Characterization on Ir(ppy)₂(Ln)@bio-MOF

3.2.1 SEM and fluorescence microscopy images

For a visual understanding on the as-synthesized supporting matrix bio-MOF-1 and Ir(ppy)₂(Ln)@bio-MOF composite samples, their SEM images are shown in Figure 3. Rod-shaped hexagonal nanocrystals are observed for the as-synthesized bio-MOF-1. Each nanocrystal is clean and intact, with average length of 40 μm. As for Ir(ppy)₂(Ln)@bio-MOF composite samples, most nanocrystals have preserved their hexagonal shape, but many nanocrystal fragments are observed as well. It seems that some long fragile nanorods have been broken into short ones or even fragments during loading procedure. There are no new clusters or sub-nanocrystals on/in Ir(ppy)₂(Ln)@bio-MOF nanocrystals, indicating that Ir(ppy)₂(Ln) molecules have been uniformly doped into bio-MOF-1 instead of being crystalized together. This hypothesis is confirmed by the fluorescence microscopy images of Ir(ppy)₂(Ln)@bio-MOF

composite samples. Uniform bluish green is observed from the whole surface of each nanocrystal, as shown in Figure 3, with no isolated $\text{Ir}(\text{ppy})_2(\text{Ln})$ nanocrystals, which tentatively confirms the successful $\text{Ir}(\text{ppy})_2(\text{Ln})$ loading in bio-MOF-1 matrix.

3.2.2 XRD and N_2 adsorption/desorption

As for the as-synthesized bio-MOF-1, its structure has been fully described by Rosi and coworkers [20]. For a confirmation on its identity, the XRD and adsorption/desorption isotherms are shown in Figure 4 and discussed below. The XRD patterns of the as-synthesized bio-MOF-1 and $\text{Ir}(\text{ppy})_2(\text{Ln})@$ bio-MOF composite samples are compared with that of standard bio-MOF-1 sample. For comparison convenience, XRD patterns of $\text{Ir}(\text{ppy})_2(\text{Ln})$ crystals are shown in Figure 4 as well. As shown in Figure 4, the as-synthesized bio-MOF-1 has shown nearly identical XRD peaks with those of standard bio-MOF-1 sample within 2θ region of 5° - 30° , which confirms the successful synthesis of supporting matrix bio-MOF-1. After loading $\text{Ir}(\text{ppy})_2(\text{Ln})$ dopant, these XRD peaks have been preserved, with no new peaks, or spectral shift, or spectral split. This result suggests that $\text{Ir}(\text{ppy})_2(\text{Ln})$ molecules are merely trapped into bio-MOF-1 matrix without changing its backbone or structure. There are no diffraction peaks from $\text{Ir}(\text{ppy})_2(\text{Ln})$ crystals. This is because dopant molecules are doped into bio-MOF-1 matrix in solution via ionic exchange procedure, thus dopant molecules are uniformly distributed in the whole matrix, instead of being crystallized.

The micropores in the as-synthesized bio-MOF-1 and $\text{Ir}(\text{ppy})_2(\text{Ln})@$ bio-MOF composite samples are determined by their N_2 adsorption/desorption isotherms shown

in Figure 4. For all three samples, Type-I isotherms have been observed, regardless of their different adsorption volume values. This result is consistent with the above statement that $\text{Ir(ppy)}_2(\text{Ln})$ dopant is merely trapped into bio-MOF-1 matrix without changing its backbone or structure. The porous parameters of bio-MOF-1 are determined as $801.4 \text{ m}^2/\text{g}$ (surface area), $0.48 \text{ cm}^3/\text{g}$ (pore volume) and 2.07 nm (pore size), respectively. They are found comparable to literature values of standard bio-MOF-1 samples ($\sim 750 \text{ m}^2/\text{g}$, $\sim 0.4 \text{ cm}^3/\text{g}$ and $\sim 2 \text{ nm}$, respectively) [23]. Combined with the above XRD result, the successful synthesis of bio-MOF-1 supporting matrix is thus confirmed. After loading $\text{Ir(ppy)}_2(\text{Ln})$, an obvious decrease in porous parameters is observed for both $\text{Ir(ppy)}_2(\text{Ln})$ samples. Their porous parameters are determined as $561.2 \text{ m}^2/\text{g}$, $0.25 \text{ cm}^3/\text{g}$ and 1.71 nm for $\text{Ir(ppy)}_2(\text{L1})@$ bio-MOF, $672.1 \text{ m}^2/\text{g}$, $0.38 \text{ cm}^3/\text{g}$ and 1.95 nm for $\text{Ir(ppy)}_2(\text{L2})@$ bio-MOF, respectively. Clearly, $\text{Ir(ppy)}_2(\text{Ln})$ molecules are filled into the micropores of bio-MOF-1, leading to these shrunk porous parameters. The comparison between adsorption volume values of $\text{Ir(ppy)}_2(\text{L1})@$ bio-MOF and $\text{Ir(ppy)}_2(\text{L2})@$ bio-MOF suggests that the doping content in $\text{Ir(ppy)}_2(\text{L1})@$ bio-MOF is higher than that in $\text{Ir(ppy)}_2(\text{L2})@$ bio-MOF. Although the bigger cell size of $\text{Ir(ppy)}_2(\text{L1})$ makes it harder to be doped into bio-MOF-1, $\text{Ir(ppy)}_2(\text{L1})$ loading level is still higher in $\text{Ir(ppy)}_2(\text{L1})@$ bio-MOF than $\text{Ir(ppy)}_2(\text{L2})$ loading level in $\text{Ir(ppy)}_2(\text{L2})@$ bio-MOF.

3.2.3 $\text{Ir(ppy)}_2(\text{Ln})$ loading content in $\text{Ir(ppy)}_2(\text{Ln})@$ bio-MOF

It is assumed that the ionic exchange rate difference between $\text{Ir(ppy)}_2(\text{L1})$ and $\text{Ir(ppy)}_2(\text{L2})$ shall be responsible for the different loading contents in $\text{Ir(ppy)}_2(\text{Ln})$

samples. To strengthen this statement, ICP measurement is performed on $\text{Ir(ppy)}_2(\text{Ln})$. Elemental content values of Zn and Ir are determined as 120.8 ppm and 31.3 ppm in $\text{Ir(ppy)}_2(\text{L1})$, 140.1 ppm and 16.2 ppm in $\text{Ir(ppy)}_2(\text{L2})$, respectively. After consulting the molecular formula of bio-MOF-1 ($\text{Zn}_8(\text{ad})_4(\text{BPDC})_6\text{O} \cdot 2\text{Me}_2\text{NH}_2$) and the ionic exchange ratio between Me_2NH_2^+ and $\text{Ir(ppy)}_2(\text{Ln})$ (1:1), the loading content values (against total Me_2NH_2^+ amount) are determined as 35.3% in $\text{Ir(ppy)}_2(\text{L1})$ and 15.7% in $\text{Ir(ppy)}_2(\text{L2})$, respectively. Although $\text{Ir(ppy)}_2(\text{L1})$ and $\text{Ir(ppy)}_2(\text{L2})$ shall have similar performance when facing the molecular sieving effect of bio-MOF-1 micropores, their ionic exchange efficiency is rather different. It is clear that $\text{Ir(ppy)}_2(\text{L1})$ is more efficient during ionic exchange procedure. This is because the counterion of $\text{Ir(ppy)}_2(\text{L1})$ (PF_6^-) is a pure one and not involved in the coordination center, serving as a pure counterion, which endows $\text{Ir(ppy)}_2(\text{L1})$ with a high mobility during ionic exchange procedure. In $\text{Ir(ppy)}_2(\text{L2})$, the Cl atom coordinates with Ir(III) center, serving as both a counterion and a ligand, which thus compromises $\text{Ir(ppy)}_2(\text{L2})$ mobility during ionic exchange procedure. These two loading contents are found both lower than literature values, though [5,23]. This is because the as-synthesized bio-MOF-1 nanocrystals are large ones ($\sim 40 \mu\text{m}$) with regular hexagonal morphology. While literature supporting matrixes usually have smaller size and higher surface-area-to-volume ratio, which makes them more efficient in ionic exchange and loading dopant.

3.3 Photophysical performance of $\text{Ir(ppy)}_2(\text{Ln})$ and $\text{Ir(ppy)}_2(\text{Ln})@$ bio-MOF

3.3.1 Absorption and excitation

The discussion on photophysical performance of $\text{Ir(ppy)}_2(\text{Ln})$ and $\text{Ir(ppy)}_2(\text{Ln})@$ bio-

MOF begins with their absorption and excitation spectra, as shown in Figure 5. Their detailed photophysical parameters are summarized in Table 4 for comparison convenience. Ir(ppy)₂(L1) and Ir(ppy)₂(L2) have shown rather similar absorption spectra, owing to their similar molecular structures. There are a major absorption band peaking at ~238 nm and two shoulder bands at ~320 nm and ~366 nm, respectively. With the ligand absorption spectra and DFT calculation result on hand, the major absorption band is attributed to the spin-allowed π - π^* transitions of ligands in Ir(ppy)₂(Ln). While the two shoulder absorption bands are newly generated ones with absorption edge of ~405 nm. Since the absorption spectra of pure ligands end at UV region (<325 nm), these two shoulder absorption bands are assigned as spin-allowed MLCT transitions of Ir(ppy)₂(Ln). After a comparison with Ir(ppy)₂(Ln) excitation spectra shown in Figure 5, it is found that regardless of its strong absorption intensity, the spin-allowed π - π^* transition (~238 nm) is inefficient in exciting Ir(ppy)₂(Ln) emission. On the other hand, the MLCT transitions are highly efficient in exciting Ir(ppy)₂(Ln) emission, showing a wide excitation band ranging from 300 nm to 400 nm. This is because the onset electronic transition of Ir(ppy)₂(Ln) is MLCT transition, which means that this MLCT-absorbed energy can be directly transferred to the emissive center (MLCT excited state), leading to its high efficiency. While, the spin-allowed π - π^* -absorbed energy has to pass a series of energy-wasting procedures before transferring its energy to the emissive center, such as geometric relaxation, potential surface crossing and so on.

As for Ir(ppy)₂(L1)@bio-MOF and Ir(ppy)₂(L2)@bio-MOF, their absorption spectra

are basically the absorption combination of dopant $\text{Ir}(\text{ppy})_2(\text{Ln})$ and supporting matrix bio-MOF-1, as shown in Figure 5. There are no newly-generated absorption bands or even obvious spectral shifts, compared to the absorption spectra of $\text{Ir}(\text{ppy})_2(\text{Ln})$ and bio-MOF-1. It is thus concluded that there is no strong interaction between $\text{Ir}(\text{ppy})_2(\text{Ln})$ molecules and bio-MOF-1 matrix. $\text{Ir}(\text{ppy})_2(\text{Ln})$ molecules are merely trapped into the micropores of bio-MOF-1 via physical adsorption effect, instead of chemical bonds or static interaction. Similar to the case of pure $\text{Ir}(\text{ppy})_2(\text{Ln})$, the excitation spectra of $\text{Ir}(\text{ppy})_2(\text{L1})@$ bio-MOF and $\text{Ir}(\text{ppy})_2(\text{L2})@$ bio-MOF fall in the weak absorption region from 300 nm to 400 nm. This excitation window has slim overlap with the excitation window of bio-MOF-1 ranging from 230 nm to 350 nm. For later emission discussion, excitation wavelength is fixed as 390 nm to avoid the excitation of bio-MOF-1 matrix.

3.3.2 Emission

Figure 6 shows the emission spectra of $\text{Ir}(\text{ppy})_2(\text{Ln})$ and $\text{Ir}(\text{ppy})_2(\text{Ln})@$ bio-MOF, along with that of supporting matrix bio-MOF-1. Owing to the large size of π chain in bio-MOF-1, a strong emission band peaking at 397 nm is observed. This emission has been assigned as the radiative decay of π - π^* transitions. Its emissive lifetime is as short as several nanoseconds and thus not quenchable by O_2 molecules, which makes it inappropriate for oxygen sensing [23]. To avoid its negative effect on later oxygen sensing, the excitation wavelength of $\text{Ir}(\text{ppy})_2(\text{Ln})$ and $\text{Ir}(\text{ppy})_2(\text{Ln})@$ bio-MOF is fixed as 390 nm which is longer than the cutting edge of bio-MOF-1 excitation wavelength (355 nm), so that dopant $\text{Ir}(\text{ppy})_2(\text{Ln})$ can be effectively excited, with supporting matrix bio-MOF-1 unexcited. As for $\text{Ir}(\text{ppy})_2(\text{L1})$, there are four emission bands, a major one

peaking at 505 nm and three weak ones peaking at 411 nm, 463 nm and 526 nm, respectively. The major emission band (505 nm) and its shoulder band (526 nm) have been widely reported for similar ppy-based phosphorescent Ir(III) complexes, which have been assigned as the emissive decay of $^3\text{MLCT}$ [21]. The other two emission bands, however, have never been reported for ppy-based phosphorescent Ir(III) complexes. After consulting the DFT calculation result, they are tentatively assigned as the emissive decay of $^3\text{MLLCT}$ (metal-to-ligand-ligand-charge-transfer). Obviously, L1 ligand participates in such emission procedure. Considering the relative intensity of these emission bands, it is clear that there is an energy competing procedure between $^3\text{MLCT}$ and $^3\text{MLLCT}$ excited states. As for $\text{Ir}(\text{ppy})_2(\text{L2})$, a broad emission band peaking at ~ 488 nm is observed. Regardless of its similar molecular structure with $\text{Ir}(\text{ppy})_2(\text{L1})$, $\text{Ir}(\text{ppy})_2(\text{L2})$'s emission is too weak to tell vibronic progressions. It is assumed that the excited state of $\text{Ir}(\text{ppy})_2(\text{L2})$ suffers from intense geometric relaxation due to the limited steric hindrance of L2 ligand.

After being doped into bio-MOF-1 matrix, $\text{Ir}(\text{ppy})_2(\text{L2})$ emission is obviously increased in $\text{Ir}(\text{ppy})_2(\text{L2})@\text{bio-MOF}$, showing a major band peaking at 483 nm and two shoulder ones peaking at 450 nm and 507 nm, respectively. Although $\text{Ir}(\text{ppy})_2(\text{L2})@\text{bio-MOF}$ still shows one major band and three shoulder bands, like $\text{Ir}(\text{ppy})_2(\text{L1})$, the relative emission intensity of these shoulder bands is decreased. Emission blue shift is observed for $\text{Ir}(\text{ppy})_2(\text{Ln})@\text{bio-MOF}$, compared to the emission of $\text{Ir}(\text{ppy})_2(\text{Ln})$, as depicted by Table 4. This observation can be explained by rigidochromism, which means that the excited state of $\text{Ir}(\text{ppy})_2(\text{Ln})$ molecules has been

protected and immobilized by bio-MOF-1 matrix. With the non-radiative decay procedures depressed, such as geometric relaxation and structural distortion, the emission shall be blue shifted and strengthened. Additionally, the weak emission bands around 400 nm are greatly decreased in Ir(ppy)₂(L1)@bio-MOF, compared to the emission bands of Ir(ppy)₂(L1). This fact suggests that ³MLLCT transition oscillation has been weakened and its energy has been transferred to ³MLCT.

3.3.3 Lifetime and quantum yield

For a better understanding on the emission feature of Ir(ppy)₂(Ln) and Ir(ppy)₂(Ln)@bio-MOF, their emission lifetimes and quantum yields are determined and listed in Table 4. It is observed from Figure 6 that Ir(ppy)₂(Ln) and Ir(ppy)₂(Ln)@bio-MOF follow monoexponential decay mode with lifetime of microseconds. The phosphorescent nature of their emission is thus confirmed. Their dominant emissive center shall be attributed to ³MLCT. Ir(ppy)₂(L2)'s weak emission matches with its low emission quantum yield of 0.01. After being doped into bio-MOF-1 matrix, both emission lifetime and quantum yield are obviously improved. This observation suggests that the non-radiative decay procedure of Ir(ppy)₂(Ln) and Ir(ppy)₂(Ln)@bio-MOF, such as geometric relaxation, structural distortion and surrounding environment quenching, has been limited, so that the energy competing for their emissive center is decreased, leading to improved emission quantum yield and longer lifetime. Generally, the radiative and non-radiative decay probability constants (K_r and K_{nr}) can be determined by Formula 1 and Formula 2. Here τ and Φ stand for emission lifetime and quantum yield, respectively.

$$\tau = 1 / (K_r + K_{nr}) \quad (1)$$

$$\Phi = K_r / (K_r + K_{nr}) \quad (2)$$

These formulas, however, are not applicable for Ir(ppy)₂(Ln) and Ir(ppy)₂(Ln)@bio-MOF. This is because there are multiple emissive centers and energy transfer procedures between them, as above mentioned. As a consequence, there are multiple radiative decay constants and non-radiative ones and shall not be determined by Formula 1 and Formula 2. Never the less, it can be sure that the supporting matrix bio-MOF-1 plays a positive role in Ir(ppy)₂(Ln)@bio-MOF. The longer emission lifetime guarantees more collision chances between Ir(ppy)₂(Ln) probe and O₂ molecules, favoring oxygen sensing.

3.4 Oxygen sensing performance of Ir(ppy)₂(Ln)@bio-MOF

3.4.1 Emission spectral response

After confirming the phosphorescent nature of Ir(ppy)₂(Ln)@bio-MOF emission, corresponding oxygen sensing performance is explored. The emission spectra of Ir(ppy)₂(Ln)@bio-MOF upon increasing O₂ concentrations are shown in Figure 7. It is observed that Ir(ppy)₂(L1)@bio-MOF emission is obviously quenched by O₂, with emission intensity decreased dramatically. On the other hand, the emission spectral band shape is well preserved, no relative intensity variation is observed between these emissive centers, indicating that these ³MLCT and ³MLLCT excited states are all quenchable by O₂ molecules. This result actually suggests a dynamic quenching mechanism, which means that O₂ molecules accept the energy from ³MLCT and ³MLLCT excited states and thus quench their emission. There is no obvious difference

between the O₂ quenching performance of these ³MLCT and ³MLLCT excited states. This is because the excited electrons are localized on the unoccupied frontier molecular orbitals which are basically the ligand π* orbitals, endowing ³MLCT and ³MLLCT excited states with rather similar O₂ sensing performance. Similar case is observed for Ir(ppy)₂(L2)@bio-MOF, showing obvious O₂ sensing behavior. Its ³MLLCT excited state (450 nm) shows a higher sensing response at low O₂ concentrations (0%-20%). This is because Ir(ppy)₂(L2) has a small ligand of halogen Cl atom, and this small steric hindrance makes the O₂ attack more easy to go, leading to the higher sensing response at low O₂ concentrations.

3.4.2 Sensitivity and Stern-Volmer working curve

For a better evaluation on the sensing performance of Ir(ppy)₂(Ln)@bio-MOF, oxygen sensing sensitivity is defined as the ratio of I₀/I₁₀₀, where I₀ means the emission intensity upon O₂ concentration of 0%, while I₁₀₀ means that upon O₂ concentration of 100%. The sensitivity values of Ir(ppy)₂(Ln)@bio-MOF are shown in Table 5. Both sensitivity values are found higher than literature values of similar oxygen sensing systems based on Cu(I) complexes and rare-earth complexes [24-26]. The following two reasons should be claimed responsible for this improvement. First, the emission lifetime of Ir(ppy)₂(Ln)@bio-MOF is at the scale of microsecond, which gives O₂ molecules enough collision chances with Ir(ppy)₂(Ln)@bio-MOF excited state. A complete quenching can be expected, favoring sensitivity. Second, Ir(ppy)₂(Ln)@bio-MOF excited state is composed of ³MLCT and ³MLLCT. Their excited electrons are localized on the outer π* orbitals of ligands, and thus vulnerable to O₂ attack. It is

observed that the I_0/I_{100} of $\text{Ir(ppy)}_2(\text{L1})@\text{bio-MOF}$ (23.65) is slightly higher than that of $\text{Ir(ppy)}_2(\text{L2})@\text{bio-MOF}$ (21.79). This observation is consistent with the longer emission lifetime of $\text{Ir(ppy)}_2(\text{L1})@\text{bio-MOF}$ than that of $\text{Ir(ppy)}_2(\text{L2})@\text{bio-MOF}$ since a longer lifetime endows O_2 molecules with more collision chances with $\text{Ir(ppy)}_2(\text{Ln})@\text{bio-MOF}$ excited state.

Generally, if a luminescent sensing probe follows a dynamic sensing mechanism, its sensing behavior can be described by Stern-Volmer equation, and the emission intensity form can be expressed by Formula 3, where I_0 means the intrinsic emission intensity in the absence of quencher, I means emission intensity, K_{sv} is Stern-Volmer fitting constant and $[\text{O}_2]$ denotes oxygen concentration, respectively.

$$I_0/I = 1 + K_{sv}[\text{O}_2] \quad (3)$$

Clearly, the working curve of an ideal sensing system should be a linear one with slope of K_{sv} against $[\text{O}_2]$. Two linear-liked working curves are observed for $\text{Ir(ppy)}_2(\text{Ln})@\text{bio-MOF}$, as shown in Figure 8. These linear working curves are found better than the non-linear ones of the sensing systems based on silica molecular sieves, such as MCM-41 and SBA-15 [12-17]. This is because supporting matrix bio-MOF-1 has long-range highly ordered micropores, which allows fluent O_2 diffusion and transportation. This observation actually confirms that $\text{Ir(ppy)}_2(\text{Ln})$ molecules have been uniformly dispersed in bio-MOF-1 matrix, which is consistent with the observation of Figure 3.

3.4.3 Response/recovery time

For a direct evaluation on the dependence between $\text{Ir(ppy)}_2(\text{Ln})@\text{bio-MOF}$ emission

quenching and O₂, Ir(ppy)₂(Ln)@bio-MOF emission is monitored with surrounding atmosphere periodically switched between pure O₂ and pure N₂. It is observed from Figure 8 that upon pure O₂ atmosphere, Ir(ppy)₂(Ln)@bio-MOF emission is quickly quenched to its minimal level and then preserved. When the surrounding atmosphere is switched to pure N₂, Ir(ppy)₂(Ln)@bio-MOF emission is gradually recovered to its maximal level and then preserved, showing a good photostability. Such procedure can be repeated at least for three cycles, indicating a good repeatability of Ir(ppy)₂(Ln)@bio-MOF sensing signal. For comparison convenience, response time is defined as the time taken by Ir(ppy)₂(Ln)@bio-MOF to lose 95% of its initial emission intensity and remain constant when surrounding atmosphere is switched from pure N₂ to pure O₂. Similarly, recovery time is defined as the time taken by Ir(ppy)₂(Ln)@bio-MOF to recover to 95% of its final emission intensity and remain constant when surrounding atmosphere is switched from pure O₂ to pure N₂. The response and recovery time values of Ir(ppy)₂(Ln)@bio-MOF are listed in Table 5. It is observed that these response and recovery time values are comparable to literature values. This is because the micropores in supporting matrix are as large as ~ 2 nm, which guarantees fluent O₂ diffusion and transportation, leading to a fast sensing response. Similar to literature case, the recovery time is much longer than the response time, which shall be explained by a diffusion-controlled dynamic procedure [13,14]. The response/recovery time values of Ir(ppy)₂(L1)@bio-MOF are exactly the same with those of Ir(ppy)₂(L2)@bio-MOF. This observation indicates that the response and recovery behavior is actually controlled by the supporting matrix, instead of dopant.

3.4.4 Quenching mechanism

We decide to discuss the quenching mechanism of Ir(ppy)₂(Ln)@bio-MOF towards O₂. For most oxygen sensing systems based on sensing probe of luminescent transition metal complexes such as Cu(I), Ru(II) and RE, the sensing mechanism is revealed as the energy quenching of their excited state via a dynamic collision with O₂ molecules [24-27]. Our above discussion has tentatively confirmed this dynamic sensing mechanism as well. On the other hand, there has been another possibility. A literature reported an oxygen sensing mechanism via the energy transfer between triplet bio-MOF and RE-based emitter [27]. But this possibility can be eliminated in Ir(ppy)₂(Ln)@bio-MOF since we use excitation wavelength of 390 nm, which is longer than the cutting edge of bio-MOF-1 excitation wavelength (355 nm) so that bio-MOF-1 can not be excited. In this case, Ir(ppy)₂(Ln)@bio-MOF sensing mechanism should be a direct quenching on Ir(ppy)₂(Ln) via a dynamic sensing mechanism. To confirm this hypothesis, Ir(ppy)₂(Ln)@bio-MOF emission lifetime is recorded under various O₂ concentrations. The lifetime values are determined as 4.66 μs upon pure N₂, 0.83 μs upon air atmosphere and 0.33 μs upon pure O₂ for Ir(ppy)₂(L1)@bio-MOF, and 2.60 μs upon pure N₂, 0.65 μs upon air atmosphere and 0.29 μs upon pure O₂ for Ir(ppy)₂(L2)@bio-MOF, respectively. The decreasing emission lifetime upon increasing O₂ concentration finally confirms the dynamic sensing mechanism of Ir(ppy)₂(Ln)@bio-MOF.

3.4.5 Humidity effect on sensing performance

For all O₂ sensors, the humidity effect on sensing signal should be considered since

H₂O should be an emission killer. The atmosphere-controlling gas was saturated with water steam (relative humidity=100%, 20°C), with corresponding emission spectra of Ir(ppy)₂(Ln)@bio-MOF shown in Figure 10. There is no obvious spectral shift or band shape change upon water steam. On the other hand, the absolute emission intensity of Ir(ppy)₂(Ln)@bio-MOF is weakened by ~10% in the presence of water steam. Two linear-liked working curves are still observed, with slightly decreased sensitivity and K_{sv}, which are fitted as 23.39 and 0.227 O₂%⁻¹ for Ir(ppy)₂(L1)@bio-MOF, 20.84 and 0.200 O₂%⁻¹ for Ir(ppy)₂(L2)@bio-MOF, respectively. It is observed that humidity effect on Ir(ppy)₂(L2)@bio-MOF is more obvious than that on Ir(ppy)₂(L1)@bio-MOF. This is because ligand L1 has a large steric hindrance and thus a better protecting on the emissive center. Ligand L2 fails to fully protect its emissive center, leading to compromised emission and sensing performance. Nevertheless, humidity effect on sensing performance is limited and acceptable.

4. Conclusion

As a conclusion, we synthesized two phosphorescent Ir(III) complexes using 2-phenyl pyridine (ppy) as the first ligand and two phosphorous ligands (L1 and L2) as the auxiliary ligand. Their successful synthesis was confirmed by their single crystals. Their phosphorescent emission was confirmed by a detailed discussion about photophysical parameters. These phosphorescent Ir(III) complexes were doped into bio-MOF-1 via cationic exchange. The resulting composite samples were analyzed by SEM, fluorescence microscopy image, XRD, N₂ adsorption/desorption and ICP measurement. Their photophysical parameters, including absorption spectra, excitation

spectra, emission spectra, emission lifetime and quantum yield, were discussed in detail. Upon increasing O₂ concentrations, their emission was gradually quenched, showing oxygen sensing behavior. Linear working curves were observed for both composite samples, showing sensitivity as high as 23.65 with response/recovery time of 9/22 seconds. Humidity effect on sensing performance was limited. These parameters were found superior to literature ones based on phosphorescent Cu(I), RE(III), Ru(II) and Re(I) complexes. The sensing mechanism was revealed as a dynamic collision between Ir(ppy)₂(Ln) and O₂ molecules. It was found that the sensitivity was controlled by sensing probe. A longer emission lifetime usually lead to a higher sensitivity. On the other hand, response and recovery performance was dominated by supporting matrix, instead of sensing probe. This conclusion should be useful for the future design of oxygen sensing system based on luminescent transition metal complexes. The novelty of this work was the combination of phosphorescent Ir(III) complexes with porous bio-MOF-1, resulting in greatly improved sensitivity and linear sensing with short response time.

References

1. J. Jo, H. Y. Lee, W. J. Liu, A. Olasz, C.H. Chen, D. Lee, *J. Am. Chem. Soc.*, 2012, 134, 16000.
2. W. Guan, W. Zhou, J. Lu, C. Lu, *Chem. Soc. Rev.* 2015, 44, 6981.
3. N. Boens, V. Leen, W. Dehaen, *Chem. Soc. Rev.*, 2012, 41, 1130.
4. E. Roussakis, Z. Li, A.J. Nichols, C.L. Evans, *Angew. Chem. Int. Edit.*, 2015, 54, 8340.
5. J. Yao, M. Yang, Y. X. Duan, *Chem. Rev.*, 2014, 114, 6130.
6. C. S. He, W. P. Zhu, Y. F. Xu, T. Chen, X. H. Qian, *Anal. Chim. Acta*, 2009, 651, 227.
7. Y. Takagai, Y. Nojiri, T. Takase, W. L. Hinze, M. Butsugan, S. Igarashi, *Analyst*, 2010, 135, 1417.
8. M.Z. Ongun, M. Sahin, T. Akbal, N. Avsar, H. Karakas, K. Ertekin, D. Atilla, H. İbişoğlu, S.Z. Topal, *Spectrochim. Acta A*, 2020, 239, 118490.
9. C. Liu, H. Yu, X. Rao, X. Lv, Z. Jin, H. Qiu, *Dyes Pigments*, 2017, 136, 641.
10. Y. Xing, C. Qiao, X. Li, C. Li, H. Wang, F. Li, L. Di, Z. Yang, *RSC Adv.*, 2019, 15370.
11. T. Yoshihara, S. Murayama, S. Tobita, *Sensors-Basel*, 2015, 15, 13503.
12. B. Lei, B. Li, H. Zhang, S. Lu, Z. Zheng, W. Li, Y. Wang, *Adv. Funct. Mater.*, 2006, 16, 1883.
13. B. Lei, B. Li, H. Zhang, L. Zhang, W. Li, *J. Phys. Chem. C*, 2007, 111, 11291.
14. L. F. Shi, B. Li, *Eur. J. Inorg. Chem.*, 2009, 2294.

15. M. T. Miller, T. B. Karpishin, *Sens. Actuators, B*, 1999, 61, 222.
16. L. F. Shi, B. Li, S. M. Yue, D. Fan, *Sens. Actuators, B*, 2009, 137, 386.
17. Y. Amao, K. Miyakawa, I. Okura, *J. Mater. Chem.*, 2000, 10, 305
18. Z. Z. Zheng, Y. L. Zhou, X. Y. Li, S. Q. Liu, Z. Y. Tang, *Biosens. Bioelectron.*, 2011, 26, 3081.
19. W. J. Guan, J. Lu, W. J. Zhou, C. Lu, *Chem. Commun.*, 2014, 50, 11895.
20. Y. J. Zheng, J. Orbulescu, X. J. Ji, F. M. Andreopoulos, S. M. Pham, R. M. Leblanc, *J. Am. Chem. Soc.*, 2003, 125, 2680.
21. L. Zhang, B. Li, L. Shi, W. Li, *Opt. Mater.*, 2009, 31, 905.
22. L. Yang, F. Okuda, K. Kobayashi, K. Nozaki, Y. Tanabe, Y. Ishii, M. A. Haga, *Inorg. Chem.*, 2008, 47, 7154.
23. Y. H. Wang, B. Li, Y. H. Liu, L. M. Zhang, Q. H. Zuo, L. F. Shi, Z. M. Su, *Chem. Commun.*, 2009, 39, 5868.
24. Z. Wang, A. R. McWilliams, C. E. B. Evans, X. Lu, S. Chung, M. A. Winnik, I. Manners, *Adv. Funct. Mater.*, 2002, 12, 415
25. Y. Wang, B. Li, L. Zhang, Q. Zuo, P. Li, J. Zhang, Z. Su, *ChemPhysChem*, 2011, 12, 349.
26. Y. Wang, B. Li, L. Zhang, H. Song, *Langmuir*, 2013, 29, 1273.
27. Y. Liu, B. Li, Y. Cong, L. Zhang, D. Fan, L. Shi, *J. Lumin.* 2011, 131, 781.
28. X. Qiao, Z. Ma, L. Si, W. Ding, G. Xu, *Sens. Actuators, B*, 2019, 299, 126978.
29. X. Wang, Y. Yang, B. He, *Sens. Actuators, B*, 2017, 242, 957.

Figure 1. ORTEP plotting of Ir(ppy)₂(L1) (a) and Ir(ppy)₂(L2) (b), and crystal stacking mode of Ir(ppy)₂(L1) (c) and Ir(ppy)₂(L2) (d).

Figure 2. Graphical presentation for FMOs of Ir(ppy)₂(L1) and Ir(ppy)₂(L2). a, Ir(ppy)₂(L1) HOMO-3, b, Ir(ppy)₂(L1) HOMO-2, c, Ir(ppy)₂(L1) HOMO-1, d, Ir(ppy)₂(L1) HOMO, e, Ir(ppy)₂(L1) LUMO, f, Ir(ppy)₂(L1) LUMO+1, g, Ir(ppy)₂(L2) HOMO-3, h, Ir(ppy)₂(L2) HOMO-2, i, Ir(ppy)₂(L2) HOMO-1, j, Ir(ppy)₂(L2) HOMO, k, Ir(ppy)₂(L2) LUMO, l, Ir(ppy)₂(L1) LUMO+1.

Figure 3. SEM images of bio-MOF-1 (a), Ir(ppy)₂(L1)@bio-MOF (b) and Ir(ppy)₂(L2)@bio-MOF (c), and fluorescence microscopy images of Ir(ppy)₂(L1)@bio-MOF (d) and Ir(ppy)₂(L2)@bio-MOF (e).

Figure 4. Left chart, XRD patterns of standard bio-MOF-1, as-synthesized bio-MOF-1, Ir(ppy)₂(Ln) crystals and Ir(ppy)₂(Ln)@bio-MOF. Right chart, N₂ adsorption/desorption isotherms of the as-synthesized bio-MOF-1 and Ir(ppy)₂(Ln)@bio-MOF composite samples.

Figure 5. Left chart, absorption spectra of bio-MOF-1, Ir(ppy)₂(Ln) and Ir(ppy)₂(Ln)@bio-MOF, Inset chart: absorption spectra of ligands ppy, L1 and L2 in CHCl₃ (1 μM). Right chart, excitation spectra of bio-MOF-1, Ir(ppy)₂(Ln) and Ir(ppy)₂(Ln)@bio-MOF.

Figure 6. Left chart, emission spectra of bio-MOF-1, Ir(ppy)₂(Ln) (in CHCl₃, 1 μM) and Ir(ppy)₂(Ln)@bio-MOF, excitation wavelength=390 nm.

Figure 7. Left chart, emission spectra of Ir(ppy)₂(L1)@bio-MOF upon increasing O₂ concentrations. Right chart, emission spectra of Ir(ppy)₂(L2)@bio-MOF upon increasing O₂ concentrations.

Figure 8. Left chart, Stern-Volmer plots of Ir(ppy)₂(L1)@bio-MOF upon increasing O₂ concentrations. Right chart, emission intensity monitoring of Ir(ppy)₂(Ln)@bio-MOF with surrounding atmosphere periodically switched between pure O₂ and pure N₂.

Figure 9. Left chart, emission decay dynamics of Ir(ppy)₂(L1)@bio-MOF upon pure N₂, air and pure O₂ atmospheres. Right chart, emission decay dynamics of Ir(ppy)₂(L2)@bio-MOF upon pure N₂, air and pure O₂ atmospheres.

Figure 10. Emission spectra of Ir(ppy)₂(L1)@bio-MOF (a) and Ir(ppy)₂(L1)@bio-MOF (b) upon increasing O₂ concentrations (saturated with water steam, relative humidity=100%), and corresponding Stern-Volmer plots (c).

Scheme 1. The synthetic route for Ir(ppy)₂(L1) and Ir(ppy)₂(L2).

Table 1. Selected geometric parameters of Ir(ppy)₂(L1) and Ir(ppy)₂(L2).

Ir(ppy) ₂ (L1)				Ir(ppy) ₂ (L2)			
bond length	(Å)	bond angle	(°)	bond length	(Å)	bond angle	(°)
Ir1-N1	2.1	N1-Ir1-C1	79.6	Ir1-N1	2.1	N1-Ir1-C1	80.6
Ir1-C1	2.0	N2-Ir1-C2	79.4	Ir1-C1	2.0	N2-Ir1-C2	79.7
Ir1-N2	2.1	P1-Ir1-P2	99.2	Ir1-N2	2.1	Cl1-Ir1-P1	90.8
Ir1-C2	2.0	N1-Ir1-P1	98.6	Ir1-C2	2.0	N1-Ir1-P1	97.4
Ir1-P1	2.5	N1-Ir1-P2	93.0	Ir1-P1	2.5	N1-Ir1-C2	86.6

Ir1-P2	2.5	N2-Ir1-P1	88.6	Ir1-Cl1	2.5	N2-Ir1-Cl1	90.4
Ir1...O1	3.5	N2-Ir1-P2	98.2	cell-a	9.9	N2-Ir1-P1	99.9
cell-a	11.8	cell- α	90.0	cell-b	14.9	cell- α	90.0
cell-b	14.3	cell- β	90.0	cell-c	22.6	cell- β	90.0
cell-c	31.2	cell- γ	93.6			cell- γ	100.9

Table 2. Percentage composition of Ir(ppy)₂(L1) first four singlet transitions and related FMOs.

FMO/transition	composition (%)		
	Ir	ppy	L1
161(LUMO+1)	7.0	72.3	20.6
160(LUMO)	5.0	77.0	13.0
159(HOMO)	40.4	39.0	19.6
158(HOMO-1)	10.2	69.2	17.6
157(HOMO-2)	24.0	57.1	18.9
156(HOMO-3)	13.1	61.0	20.2
S ₀ →S ₁	MLCT, MO159→160(94.7)		
S ₀ →S ₂	MLCT, MO159→161(93.2)		
S ₀ →S ₃	MLCT, MO158→160(96.5)		
S ₀ →S ₄	MLCT, MO158→161(89.1)		

Table 3. Percentage composition of Ir(ppy)₂(L2) first four singlet transitions and related FMOs.

FMO/transition	composition (%)			
	Ir	ppy	L2	Cl
117(LUMO+1)	11.4	84.2	3.1	0.7
116(LUMO)	4.2	85.9	9.9	0.5
115(HOMO)	40.0	35.8	5.9	17.9
114(HOMO-1)	43.0	27.4	12.9	16.5
113(HOMO-2)	38.2	43.2	11.3	7.3
112(HOMO-3)	8.3	44.0	25.6	22.3
S ₀ →S ₁	MLCT, MO115→116(94.3)			
S ₀ →S ₂	MLCT, MO114→116(82.3)/113→116(10.5)			
S ₀ →S ₃	MLCT, MO115→117(91.4)			
S ₀ →S ₄	MLCT, MO114→117(69.9)/113→116(27.4)			

Table 4. Photophysical parameters of bio-MOF-1, Ir(ppy)₂(Ln) and Ir(ppy)₂(Ln)@bio-MOF.

	λ_{abs} (nm)	λ_{edg} (nm)	λ_{em} (nm)	τ (μs)	Φ
Ir(ppy) ₂ (L1),solution	238,320,366	405	411,463,505,526	0.43	0.33
Ir(ppy) ₂ (L2),solution	237,321,367	409	488 (broad)	0.29	0.01
Ir(ppy) ₂ (L1)@bio-MOF	220,247,344	414	405,458,489,511	0.83	0.60
Ir(ppy) ₂ (L2)@bio-MOF	223,258,344	414	450,483,507	0.65	0.51
bio-MOF-1	253,345	392	397	0.06	0.05

Table 5. Key sensing parameters of Ir(ppy)₂(Ln)@bio-MOF and other literal O₂ sensing systems.

	I_0/I_{100}	K_{sv} (O ₂ % ⁻¹)	linearity	response (s)	Ref.
Ir(ppy) ₂ (L1)@bio-MOF	23.65	0.223	linear	9/22	this work
Ir(ppy) ₂ (L2)@bio-MOF	21.79	0.206	linear	9/22	this work
[Cu(POP)phencarz]BF ₄ -PS	15.56	0.1492	linear	9/14	Ref. 23
[Eu(TTA) ₃ (phencarz)]/PS	3.38	$K_{sv1}, 0.0508$ $K_{sv2}, 0.1010$	non- linear	5/8	Ref. 25
Ru(bpy) ₂ Phen-MMS	5.5	$K_{sv1}, 0.0165$ $K_{sv2}, 0.4752$	non- linear	6/12	Ref. 26
D-Re(I)/MCM-41	5.6	$K_{sv1}, 0.2801$ $K_{sv2}, 0.0089$	non- linear	19/41	Ref. 27
D-Re(I)/SBA15	20.1	$K_{sv1}, 1.2872$ $K_{sv2}, 0.0054$	non- linear	7/43	Ref. 27
Eu(L3)@bio-MOF-1	6.96	0.0578	linear	16/19	Ref. 28
Ir(III) in polymer films	15.56	$K_{sv1}, 0.174$ $K_{sv2}, 0.003$	non- linear	8/24	Ref. 29

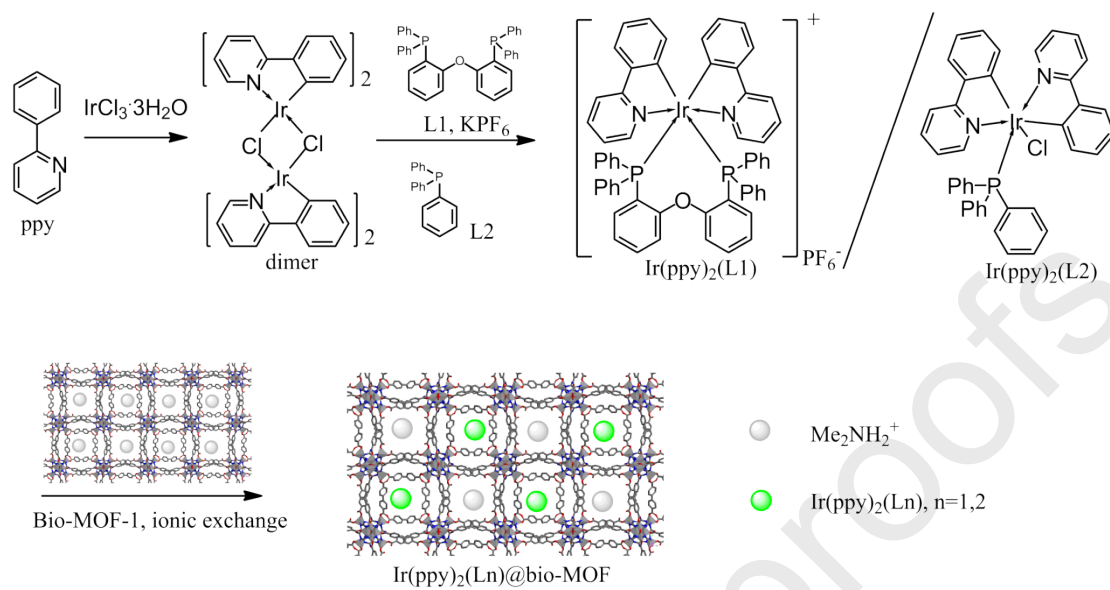
Scheme 1. The synthetic route for $\text{Ir}(\text{ppy})_2(\text{L}1)$ and $\text{Ir}(\text{ppy})_2(\text{L}2)$.

Figure 1. ORTEP plotting of $\text{Ir}(\text{ppy})_2(\text{L1})$ (a) and $\text{Ir}(\text{ppy})_2(\text{L2})$ (b), and crystal stacking mode of $\text{Ir}(\text{ppy})_2(\text{L1})$ (c) and $\text{Ir}(\text{ppy})_2(\text{L2})$ (d).

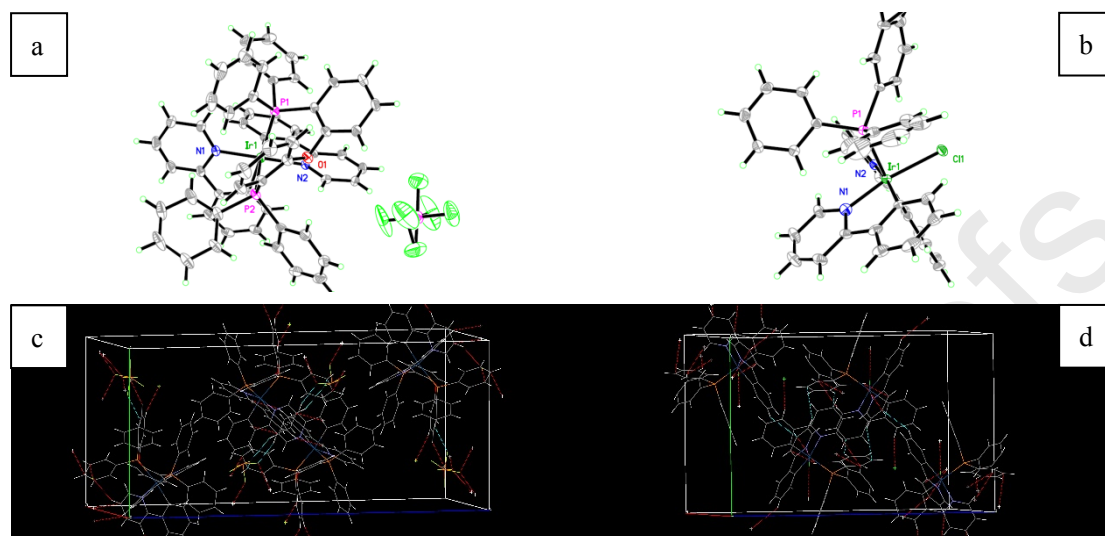


Figure 2. Graphical presentation for FMOs of $\text{Ir(ppy)}_2(\text{L1})$ and $\text{Ir(ppy)}_2(\text{L2})$. a, $\text{Ir(ppy)}_2(\text{L1})$ HOMO-3, b, $\text{Ir(ppy)}_2(\text{L1})$ HOMO-2, c, $\text{Ir(ppy)}_2(\text{L1})$ HOMO-1, d, $\text{Ir(ppy)}_2(\text{L1})$ HOMO, e, $\text{Ir(ppy)}_2(\text{L1})$ LUMO, f, $\text{Ir(ppy)}_2(\text{L1})$ LUMO+1, g, $\text{Ir(ppy)}_2(\text{L2})$ HOMO-3, h, $\text{Ir(ppy)}_2(\text{L2})$ HOMO-2, i, $\text{Ir(ppy)}_2(\text{L2})$ HOMO-1, j, $\text{Ir(ppy)}_2(\text{L2})$ HOMO, k, $\text{Ir(ppy)}_2(\text{L2})$ LUMO, l, $\text{Ir(ppy)}_2(\text{L1})$ LUMO+1.

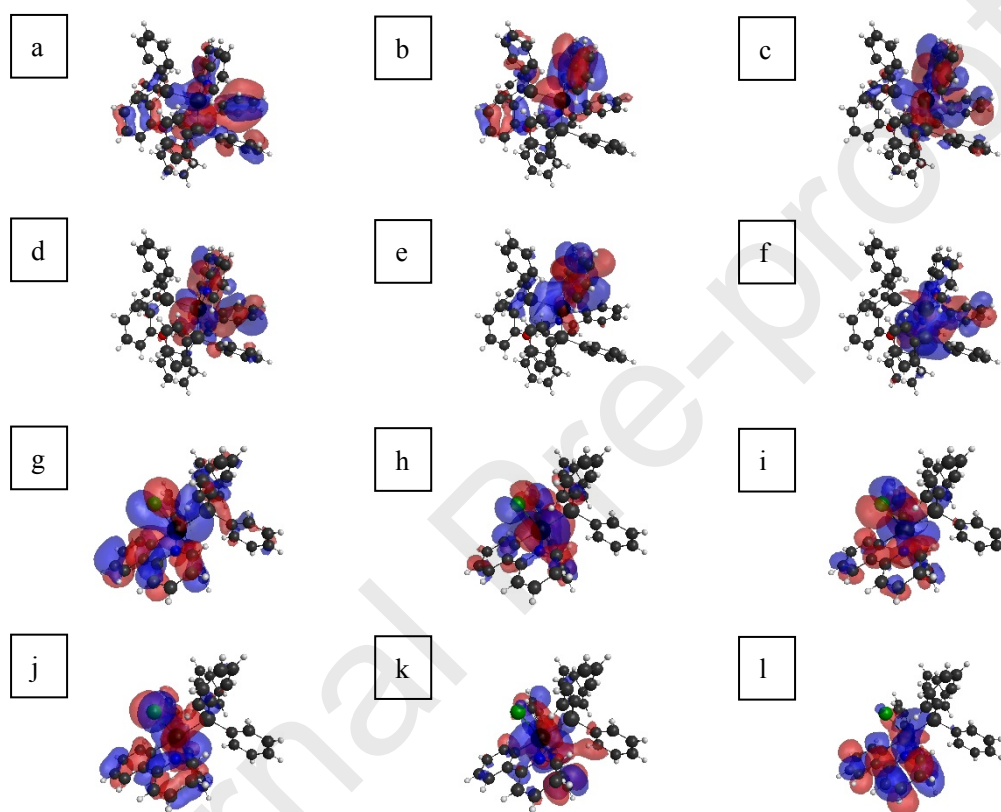


Figure 3. SEM images of bio-MOF-1 (a), Ir(ppy)₂(L1)@bio-MOF (b) and Ir(ppy)₂(L2)@bio-MOF (c), and fluorescence microscopy images of Ir(ppy)₂(L1)@bio-MOF (d) and Ir(ppy)₂(L2)@bio-MOF (e).

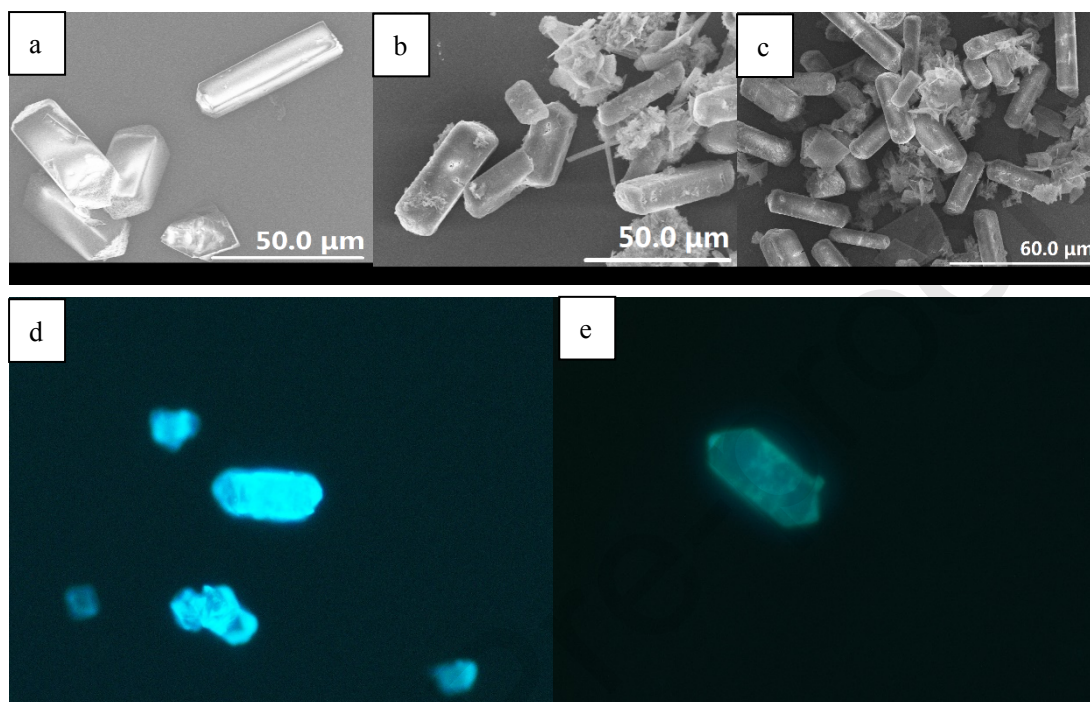


Figure 4. Left chart, XRD patterns of standard bio-MOF-1, as-synthesized bio-MOF-1, $\text{Ir(ppy)}_2(\text{Ln})$ crystals and $\text{Ir(ppy)}_2(\text{Ln})@$ bio-MOF. Right chart, N_2 adsorption/desorption isotherms of the as-synthesized bio-MOF-1 and $\text{Ir(ppy)}_2(\text{Ln})@$ bio-MOF composite samples.

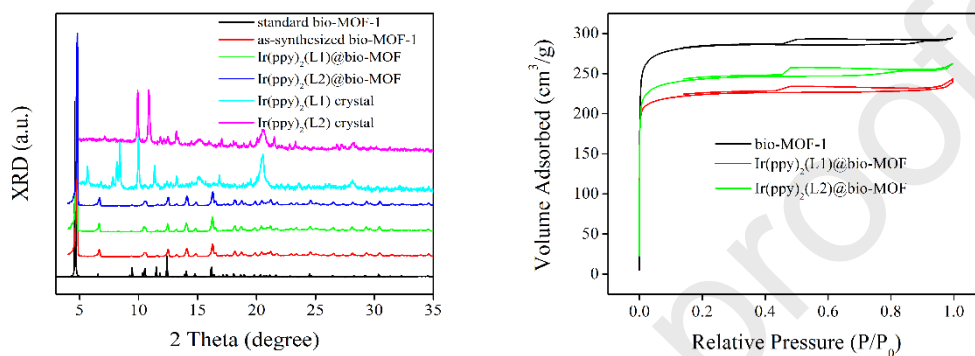


Figure 5. Left chart, absorption spectra of bio-MOF-1, $\text{Ir}(\text{ppy})_2(\text{Ln})$ and $\text{Ir}(\text{ppy})_2(\text{Ln})@$ bio-MOF, Inset chart: absorption spectra of ligands ppy, L1 and L2 in CHCl_3 (1 μM). Right chart, excitation spectra of bio-MOF-1, $\text{Ir}(\text{ppy})_2(\text{Ln})$ and $\text{Ir}(\text{ppy})_2(\text{Ln})@$ bio-MOF.

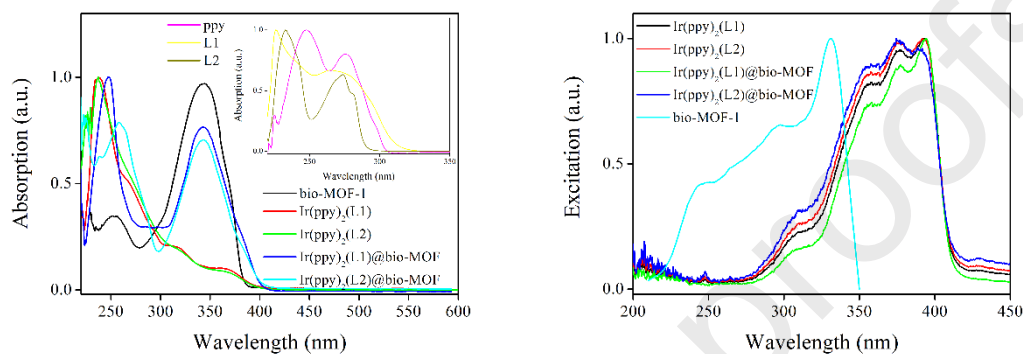


Figure 6. Left chart, emission spectra of bio-MOF-1, $\text{Ir(ppy)}_2(\text{L}_n)$ (in CHCl_3 , 1 μM) and $\text{Ir(ppy)}_2(\text{L}_n)\text{@bio-MOF}$, excitation wavelength=390 nm.

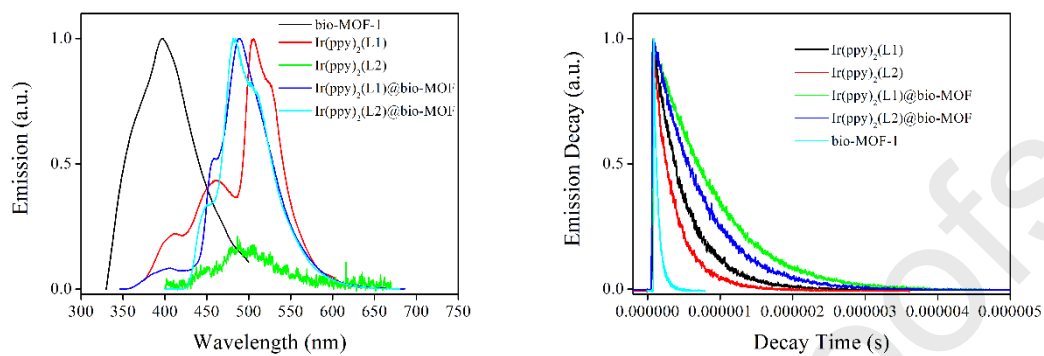


Figure 7. Left chart, emission spectra of $\text{Ir}(\text{ppy})_2(\text{L1})@\text{bio-MOF}$ upon increasing O_2 concentrations. Right chart, emission spectra of $\text{Ir}(\text{ppy})_2(\text{L2})@\text{bio-MOF}$ upon increasing O_2 concentrations.

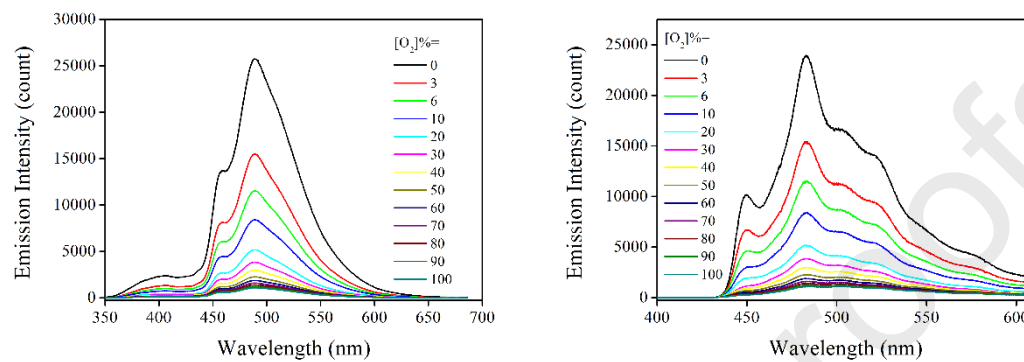


Figure 8. Left chart, Stern-Volmer plots of $\text{Ir}(\text{ppy})_2(\text{L1})@\text{bio-MOF}$ upon increasing O_2 concentrations. Right chart, emission intensity monitoring of $\text{Ir}(\text{ppy})_2(\text{Ln})@\text{bio-MOF}$ with surrounding atmosphere periodically switched between pure O_2 and pure N_2 .

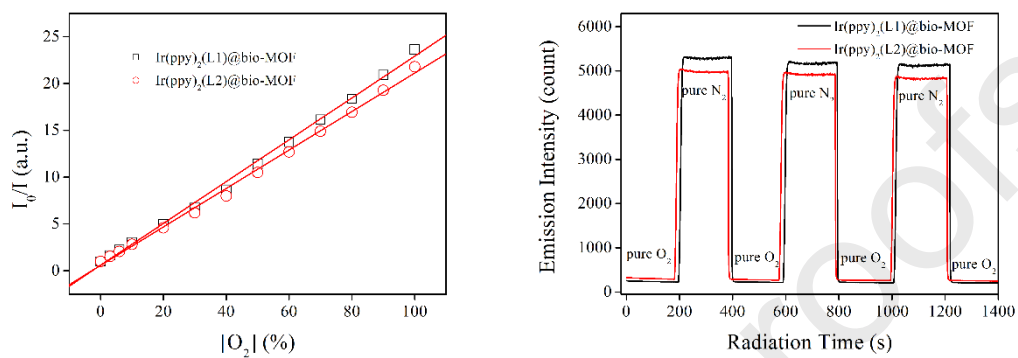


Figure 9. Left chart, emission decay dynamics of $\text{Ir(ppy)}_2(\text{L1})@\text{bio-MOF}$ upon pure N_2 , air and pure O_2 atmospheres. Right chart, emission decay dynamics of $\text{Ir(ppy)}_2(\text{L2})@\text{bio-MOF}$ upon pure N_2 , air and pure O_2 atmospheres.

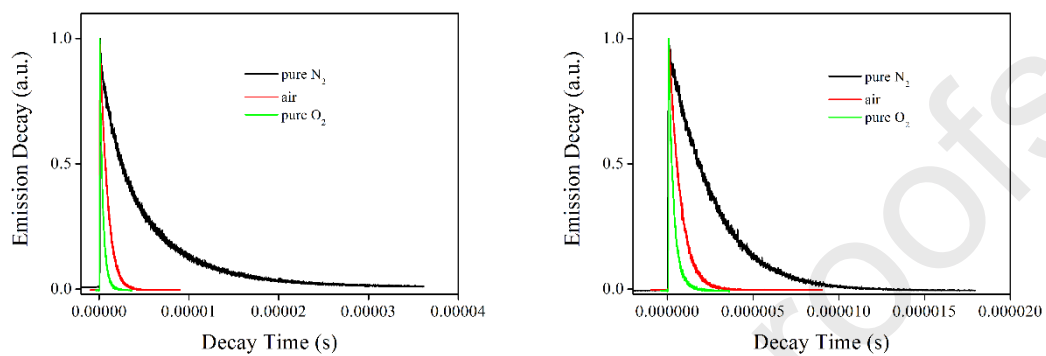
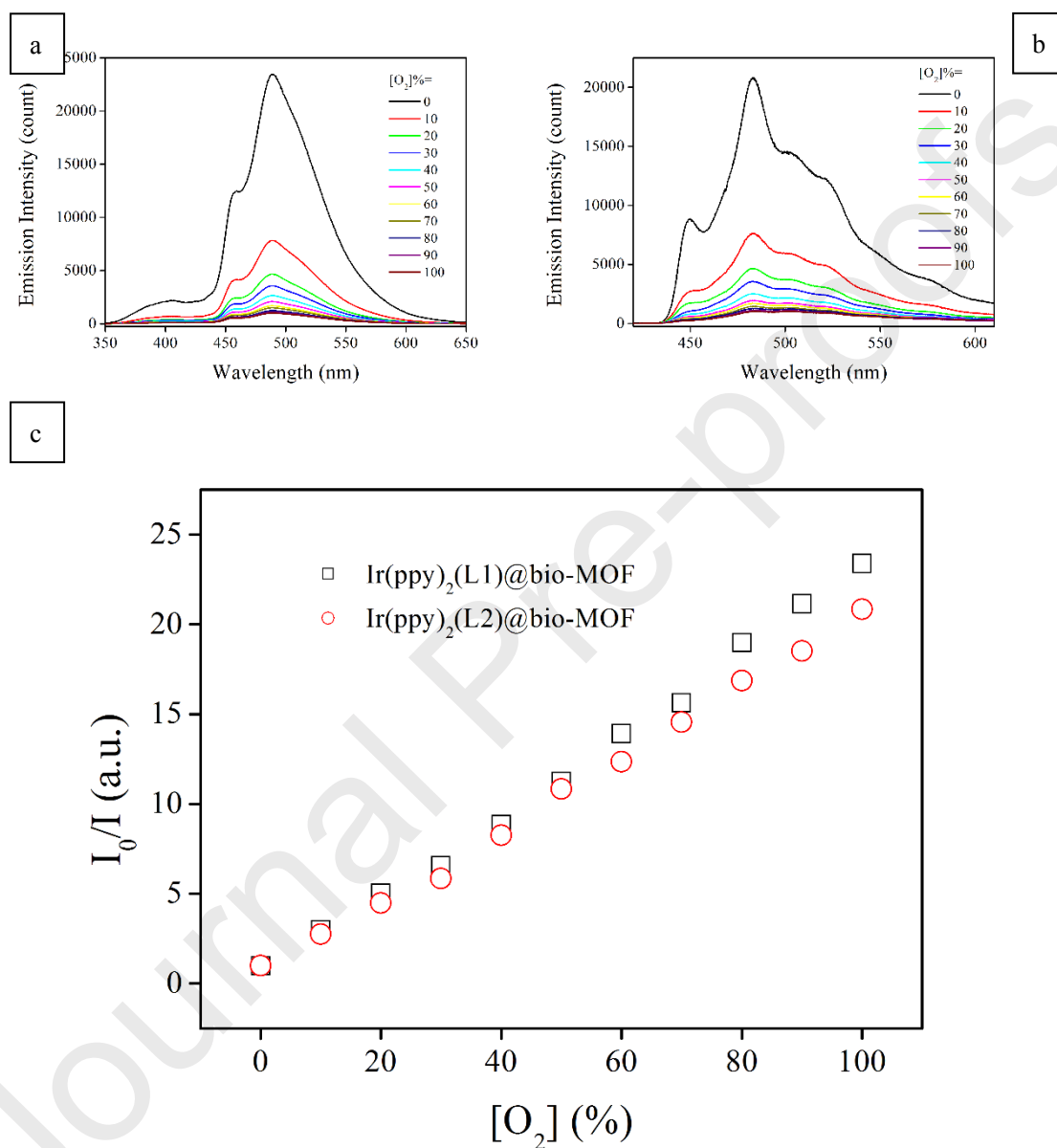
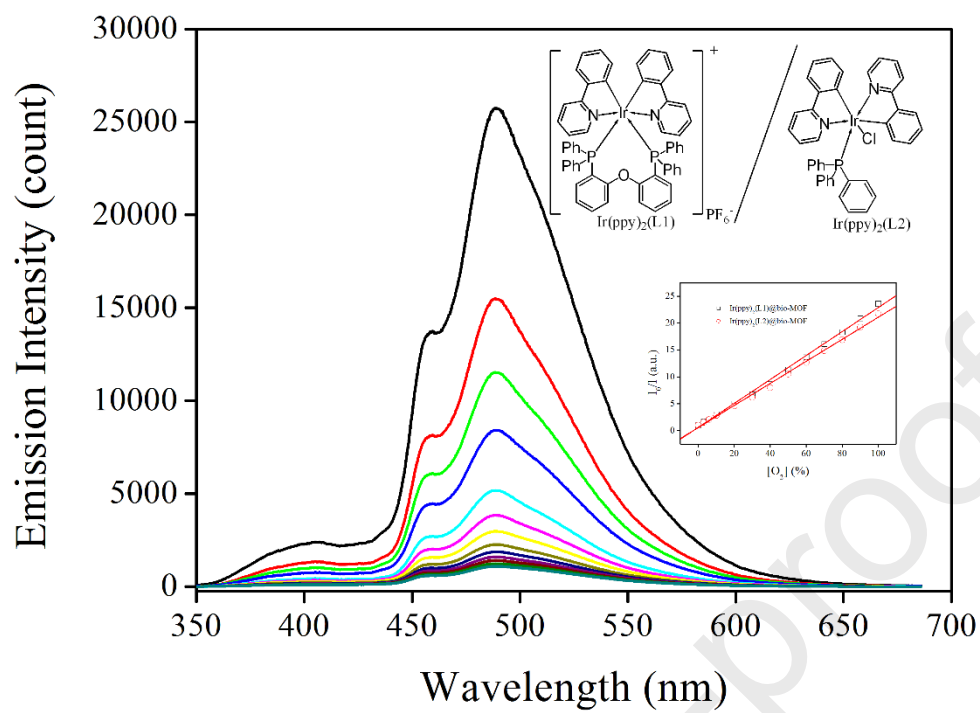


Figure 10. Emission spectra of Ir(ppy)₂(L1)@bio-MOF (a) and Ir(ppy)₂(L1)@bio-MOF (b) upon increasing O₂ concentrations (saturated with water steam, relative humidity=100%), and corresponding Stern-Volmer plots (c).



For Graphic Abstract



Journal Pre-proofs